IFASD 2015
International Forum on Aeroelasticity and Structural Dynamics
June 28 — July 02, 2015 ▲ Saint Petersburg, Russia

# DYNAMIC LOAD ALLEVIATION OF FLEXIBLE AIRCRAFT IN WAKE VORTEX ENCOUNTERS

**Henrik Hesse**[1], **Rafael Palacios**[2*]

[1] Automatic Control Laboratory, ETH, Zurich 8092, Switzerland

[2] Imperial College, London SW7 2AZ, United Kingdom

**Keywords:** Load alleviation, aeroelastic control, flexible aircraft dynamics, wake encounter

**Abstract:** This paper introduces an integrated approach for flexible-aircraft time-domain aeroelastic simulation and controller design suitable for wake encounter situations. The dynamic response of the vehicle, which may be subject to large wing deformations in trimmed flight, is described by a geometrically-nonlinear composite-beam finite-element model. The aerodynamics is modeled using the unsteady vortex lattice method and includes the arbitrary time-domain downwash distributions of a wake encounter. A consistent linearization in the structural degrees of freedom enables the use of balancing methods to reduce the problem size while retaining the nonlinear terms in the rigid-body equations. Numerical studies on a very flexible aircraft demonstrate the reduced-order modeling approach for load calculations in wake vortex encounters over a large parameter space. Closed-loop results finally explore the potential of combining feedforward/feedback $\mathcal{H}_\infty$ control and conventional control surfaces for load alleviation.

## Nomenclature

*Symbols*

| | |
|---|---|
| $b_V$ | distance between wake vortex segments |
| $\mathcal{C}$ | global tangent damping matrix |
| $\mathcal{K}$ | global tangent stiffness matrix |
| $\mathcal{M}$ | global tangent mass matrix |
| $\boldsymbol{q}$ | generalized displacements in modal basis |
| $\boldsymbol{Q}_{ext}$ | global vector of external forces |
| $r$ | distance from encountering aircraft to wake vortex |
| $t$ | physical time |
| $\boldsymbol{u}$ | input vector of a linear system identified by subscripts |
| $v$ | inertial translational velocity of the body-fixed frame |
| $\boldsymbol{w}_g$ | input vector of 3D disturbance velocities |
| $W$ | weighting matrices for control synthesis |
| $\boldsymbol{x}$ | state vector of a linear system identified by subscripts |

*Contact author. E-mail address: r.palacios@imperial.ac.uk

| | |
|---|---|
| $\boldsymbol{y}$ | output vector of a linear system identified by subscripts |
| $\boldsymbol{\beta}$ | vector of global translational and rotational velocities |
| $\boldsymbol{\Gamma}$ | vector of circulation strengths of vortex rings |
| $\boldsymbol{\eta}$ | vector of nodal displacements and rotations |
| $\boldsymbol{\Theta}$ | Euler angles, rad |
| $\Phi$ | matrix of mode shapes |
| $\boldsymbol{\chi}$ | coordinates of the aerodynamic lattice |
| $\omega$ | inertial angular velocity of the body-fixed frame |

*Subscripts*

| | |
|---|---|
| $b$ | bound, corresponding to lifting surface |
| $F$ | aerodynamic |
| $S$ | structural degrees of freedom |
| $w$ | wake |

*Superscripts*

| | |
|---|---|
| $\dot{(\bullet)}$ | derivatives with respect to time, $t$ |

# 1 Introduction

The increased wing flexibility found in latest-generation aircraft brings greater risks of aeroelastic vibrations excited during maneuvers or due to atmospheric disturbances. Dynamic load alleviation systems may provide a key enabler in their design by improving the vehicle handling qualities, suppressing structural vibrations, and reducing peak loads. The latter is increasingly relevant in wake vortex encounters (WVE), which occur when the aircraft crosses the wake of another aircraft, or even its own wake in a tight maneuver. Such encounters lead to aggressive excitations, which are especially critical in landing approach and take-off.

To avoid dangerous vehicle perturbations during landing approaches, the Federal Aviation Administration imposes a minimum separation between approaching/leaving aircraft based on their relative weight difference [1, 2]. Consequently, recent research efforts have focused on detection and prediction of wake vortices around runways to optimize the wake vortex separations between aircraft based on novel turbulence sensors and wake vortex simulations [3, 4]. On the positive side, extended formation flight takes advantage of the upwash in the wake of a preceding aircraft to significantly reduce the vehicle induced drag and fuel burn. The potential benefits for transport aircraft have been demonstrated in recent flight tests [5, 6] and numerical studies [7]. In either case, advanced flight control techniques are required to ensure optimal trajectories of the vortex-generating and the follower aircraft [8], particularly with adverse atmospheric conditions. From the point of view of airframe design, unexpected WVE can lead to large dynamic loads that create structural integrity risks. That brings a need for improved analysis methods and also of strategies for load alleviation tailored to this situation.

The modeling of WVE is a twofold problem: (a) understanding the mechanism of wake generation, topology, vortex strength, and decay and (b) identifying the parameter space of possible encounter scenarios. The development and propagation of wake vortices have been investigated in flight test experiments and simplified models of the induced

three-dimensional (3D) velocity field have been identified [9–11]. Once a pair of wake vortices is formed behind the generating aircraft, cross-induction leads to expansion, perturbation, and eventual decay of the vortex segments, as described in detail in Holzäpfel *et al.* [12] and Bieniek and Luckner [13]. Numerous flight tests by the German Aerospace Research Center (DLR) have provided significant insight into the impact of WVE on the vehicle dynamic response of the encountering (rigid) aircraft due to possible rolling moments induced by the wake vortices [9, 14, 15]. Such aggressive excitations of the vehicle dynamics can lead to critical loads on weight-optimized aircraft components. This has been demonstrated in a recent flight test campaign on the Airbus A400M, a large military transport aircraft, to measure WVE loads for different encounter angles and altitudes [16]. The tests showed that the *encounter parameters*, e.g. vertical offset or angle between the flightpaths of the generating and encountering aircraft, have a large impact on the vehicle response and dynamic loads.

This demonstrates that a comprehensive study of WVE loads in the design of future aircraft needs to incorporate a large parameter space of possible encounter scenarios, which requires many simulation cases. Moreover, WVE bring time and spatially varying excitations, with a relatively large frequency range, which needs to be tackled with an integrated aeroelastic/flight-dynamic modeling approach in time domain. This has been recently addressed by Kier [17, 18] and Karpel *et al.* [19], who have developed modeling frameworks to compute the dynamic response of flexible aircraft subject to wake encounters. In both approaches the vehicle unsteady aerodynamics are computed based on a doublet lattice method (DLM), which, in Kier's work are transformed to time-domain state-space models using rational-function approximations [20]. The unsteady aerodynamic effects were found to be significant in head-on WVE scenarios [18], where the encountering aircraft crosses the wake perpendicular to the flightpath of the originating aircraft. Kier [17] further demonstrated that for varying encounter angles, WVE can lead to significant roll and yaw excitations. The resulting change in flightpath was also found to effect the encounter loads as slight changes in the encounter geometry significantly impact the local induced velocities. Both approaches have been successfully validated against experimental data obtained for different WVE scenarios of the Airbus A400M flight test campaign [16, 19]. Further parametric studies have demonstrated that vibration modes of the large T-tail structure of the A400M, are excited in certain encounter scenarios [21].

Although DLM-based aeroelastic approaches have been successfully applied to WVE load calculations, they require curve fitting of a large parameter set for the transformation to time domain. Furthermore, DLM-based solutions assume small normal displacements of the lifting surfaces, which may be no longer valid in high-load situations typical for WVE. Time-domain aerodynamic models, such as the unsteady vortex lattice method (UVLM), provide a more flexible alternative to frequency-domain methods, although their application is limited to incompressible flows. In the UVLM, dynamic loads are evaluated on the instantaneous deformed geometry and therefore can be coupled directly to geometrically-exact flexible-body dynamic models of the maneuvering vehicle [22]. In addition, the UVLM captures the interference effects between the lifting surfaces and the non-planar wakes. This provides a higher fidelity aerodynamic solution compared to quasi-steady 3D lifting-line models or 2D unsteady strip theory typically used in transient analysis of very flexible aircraft [23, 24].

However, time-domain aeroelastic solutions expressed in terms of the instantaneous circulation in all aerodynamic panels can be too computationally expensive for control-

ler design and routine analysis of multiple load scenarios. Hence, recent work by the authors [25] has focused on model reduction of UVLM-based aeroelastic systems using balancing methods. The application of the reduced-order modeling approach for maneuvering flexible aircraft was enabled through a consistent linearization of the structural degrees of freedom (DOF) in nonlinear flexible-aircraft dynamics problems [26]. The underlying rigid-body dynamic equations of motion (EOM) however remain nonlinear. The resulting low-order modeling approach has been demonstrated for fast transient analyses of maneuvering flexible aircraft following antisymmetric control surface inputs and load calculations in spanwise non-uniform discrete gust encounters [25]. Continuing on those studies, this work will investigate the application of the reduced-order modeling approach for WVE load calculations, which is characterized by independent disturbances on each aerodynamic panel, and subsequent design of a dynamic load alleviation system based on the coupled aeroelastic/flight-dynamic vehicle description.

As mentioned above, load alleviation is especially relevant for larger and more flexible aircraft, which may be subject to large wing deformations in their flight envelopes. For active load alleviation systems to be effective on such platforms, they need to incorporate the effect of wing deformations on the vehicle stability characteristics [26]. Load reduction has been demonstrated recently by Cook *et al.* [27] and Dillsaver *et al.* [28] among others, who explored the application of $\mathcal{H}_\infty$ and LQG controllers, respectively, to full aircraft models including geometrically-nonlinear aeroelastic descriptions. In both cases the controllers have been obtained from linearized representations of the aircraft models around geometrically-nonlinear trim equilibria. The mismatch between the linear control model and the nonlinear simulation model, however, makes the tuning of such controllers difficult. Hence, Simpson *et al.* [29] recently explored model predictive control (MPC) for gust load alleviation, which includes active constraints in the on-line optimization problem. Predictive controllers also provide the opportunity to include preview information of the disturbance field ahead of the aircraft flightpath using light detection and ranging sensors (LIDAR) or probes mounted to the fuselage. LIDAR sensors increase the range of the forward measurements to 100 m, which can significantly improve the capability of feedforward control for gust rejection [9, 30–32]. This has also been demonstrated for commercial aircraft using MPC based on linear aeroelastic models [33] and for rigid aircraft using feedforward control in WVE [9, 34, 35]. Hahn *et al.* [34] further demonstrated in flight experiments the benefit of dedicated direct lift control (DLC) flaps to effectively counteract abrupt roll responses in WVE.

Forward-looking control techniques have the potential to respond to disturbance measurements much faster and ideally could suppress aerodynamic perturbations before the vehicle dynamics are affected. However, this requires substantial control authority that allows to affect the lift distribution over the whole aircraft. This has been explored by Wildschek *et al.* [32] in the design of gust load alleviation systems for blended wing body (BWB) aircraft with arrays of 12 trailing edge flaps and 12 spoilers on the upper side of the wing. For the efficient synthesis of optimal controllers for reconfigurable control surface on the BWB concept with feedforward capabilities, Westermayer *et al.* [36] proposed a $\mathcal{H}_\infty$ full information approach.

The effectiveness of feedforward control with preview on flexible aircraft heavily depends on the ability to predict the aeroelastic interactions due to the flow disturbances. To respond to aggressive excitations inherent to WVE, we will focus in this work on forward-looking multi-input, multi-output (MIMO) control techniques based on a top-down approach. A higher-fidelity aeroelastic description that captures critical features

such as large deformations at trim, nonlinear flight dynamics, and possible aerodynamic interference effects between lifting surfaces will be incorporated in the control synthesis.

The remainder of the paper is organized as follows. Firstly, we present an overview of the underlying aeroelastic formulation of maneuvering flexible aircraft. The resulting simulation model will be used to compute the dynamic loads in wake vortex encounters, as defined in Section 2.4. Consistent linearization and model reduction in Section 3 provides the control model for the design of a dynamic load alleviation system based on strain and disturbance measurements. Numerical studies in Section 4.2 exercise the aeroelastic modeling approach to compute the dynamics loads for a range of WVE scenarios. Finally, Section 4.3 presents an investigation on a simple load allevation strategy that combines feedforward and feedback $\mathcal{H}_\infty$ controllers.

# 2 Flexible-Aircraft Dynamics Simulation Model

To simulate the dynamics of flexible aircraft subject to large rigid-body motions, e.g. due to gusts or control surface inputs, we follow an integrated aeroelastic and flight-dynamics modeling approach. The system dynamics is nonlinear due to possibly large rigid-body motions of the vehicle, but we will assume small elastic deformations of lifting surfaces during the transient dynamics (the reference condition may still exhibit large displacements). Consequently, we can also assume that the unsteady aerodynamics are linear [22] and will be computed in this work using a linearized 3D UVLM. The underlying models have been implemented in Imperial College's framework for Simulation of High Aspect Ratio Planes (`SHARP`), which includes static aeroelastic analyses, trim, linear stability analyses, and fully nonlinear time-marching simulations [22, 25, 26, 37, 38]. Here, we provide a brief description of the aerodynamic and flexible-body dynamic models in Sections 2.1 and 2.2, respectively, which are used in Section 2.3 to obtain the simulation plant for the coupled flexible-aircraft dynamics. Modeling of the wake vortices, which appear as disturbance terms in the linearized UVLM, is covered in Section 2.4.

## 2.1 Unsteady Vortex Lattice Method

The unsteady aerodynamic loads in this work are obtained using the linearized UVLM developed by Murua *et al.* [22]. In the UVLM, vortex ring quadrilateral elements are used to discretize the lifting surfaces ($M_b$ chordwise and $N$ spanwise panels) and their wakes ($M_w \times N$ panels), as illustrated in Figure 1. Each surface (bound) vortex ring has an associated circulation strength, $\Gamma_k$, and a collocation point, at which the impermeability boundary condition is satisfied. To obtain the state-space form of the UVLM, the governing equations are linearized on a *frozen* aerodynamic geometry [22, 39] around the aircraft trim condition with possibly large wing deformations and non-planar wake. The resulting relations can be cast in the canonical discrete-time form

$$\Delta\boldsymbol{\Gamma}^{n+1} = A_F \Delta\boldsymbol{\Gamma}^n + B_F \Delta\boldsymbol{u}_F^n, \tag{1}$$

where superscripts $n$ and $n+1$ refer to the current and next time steps and the subscript $F$ refers to the linear time-invariant (LTI) aerodynamics. The state, $\boldsymbol{\Gamma}$, and input, $\mathbf{u}_F$, vectors are

$$\boldsymbol{\Gamma} = \begin{bmatrix} \boldsymbol{\Gamma}_b^\top & \boldsymbol{\Gamma}_w^\top & \dot{\boldsymbol{\Gamma}}_b^\top \end{bmatrix}^\top, \quad \text{and} \quad \boldsymbol{u}_F = \begin{bmatrix} \boldsymbol{\chi}_b^\top & \dot{\boldsymbol{\chi}}_b^\top & \boldsymbol{w}_g^\top \end{bmatrix}^\top, \tag{2}$$

where $\boldsymbol{\Gamma}_b \in \mathbb{R}^{K_b}$ and $\boldsymbol{\Gamma}_w \in \mathbb{R}^{K_w}$ are the bound (surface) and wake circulation strengths, respectively, where $K_b = M_b N$ and $K_w = M_w N$ are the corresponding total number of bound and wake vortex panels. The coordinates and their time-derivatives of the bound aerodynamic grid, $\boldsymbol{\chi}_b \in \mathbb{R}^{K_\chi}$ and $\dot{\boldsymbol{\chi}}_b$, respectively, include small elastic deformations of the lifting surfaces as well as the rigid-body velocities and orientation of the vehicle, where $K_\chi = (M_b+1)(N+1)$. They also include the effect of the deployment of control surfaces. Finally, $\boldsymbol{w}_g \in \mathbb{R}^{3K_b}$ refers to disturbance inputs, which appear as downwash contributions at the collocation points and account, in particular, for the 3D velocity disturbances in WVE.

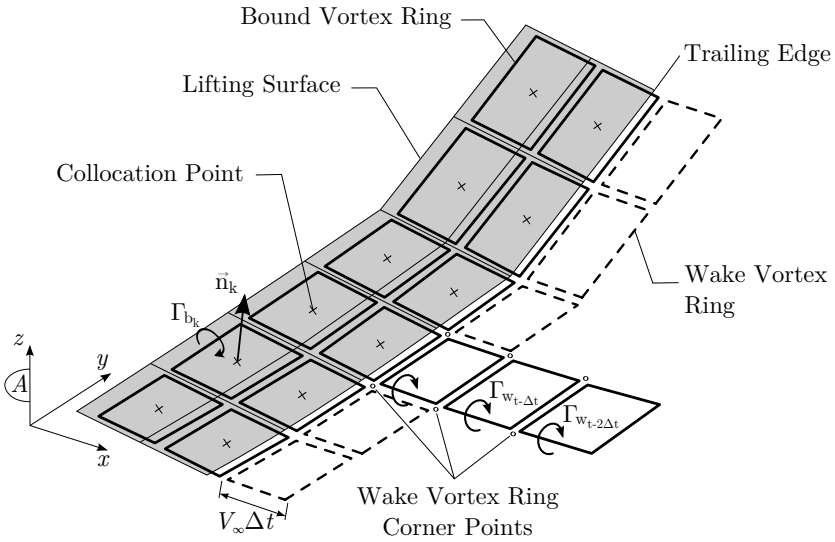



Figure 1: Unsteady vortex lattice method with vortex ring discretization of lifting surface and wake for free-stream flow in positive $x$ direction.

The unsteady aerodynamic loads at each aerodynamic panel result from the vorticity distribution at each time step and are computed using the unsteady Bernoulli equation [22, 40]. The resulting loads are the outputs of the aerodynamic system and will therefore be written as $\Delta \boldsymbol{y}_F$, which is written in symbolic form as

$$\Delta \boldsymbol{y}_F^n = C_F \Delta \boldsymbol{\Gamma}^n + D_F \Delta \boldsymbol{u}_F^n. \tag{3}$$

where the system feedthrough is included to account for the change in orientation of the aerodynamic loads which depends on the velocities, $\dot{\boldsymbol{\chi}}_b$. Note finally that $\dot{\boldsymbol{\Gamma}}_b$ was included in the state variable as it is needed to obtain the pressure field in unsteady flows.

## 2.2 Flexible-Body Dynamics Model

The flexible vehicle will be modeled using composite beam elements on a moving (body-attached) frame of reference. Starting from a geometrically nonlinear displacement-based formulation [41, 42], the elastic DOF are the displacements and rotations at the element nodes, which have been linearized using perturbation methods [38]. This consistent linearization is done around a static equilibrium (trimmed aircraft in forward flight) with possibly large elastic deformations, which will be referred to as $\boldsymbol{\eta}_0 \in \mathbb{R}^{6(n_S-1)}$, where $n_S$ is

the number of nodes in the beam description. The resulting set of perturbation equations is [26, 38]

$$\mathcal{M}(\boldsymbol{\eta}_0)\begin{Bmatrix}\Delta\ddot{\boldsymbol{\eta}}\\ \dot{\boldsymbol{\beta}}\end{Bmatrix}+\mathcal{C}(\boldsymbol{\eta}_0,\boldsymbol{\beta})\begin{Bmatrix}\Delta\dot{\boldsymbol{\eta}}\\ \boldsymbol{\beta}\end{Bmatrix}+\mathcal{K}(\boldsymbol{\eta}_0,\boldsymbol{\beta})\begin{Bmatrix}\Delta\boldsymbol{\eta}\\ 0\end{Bmatrix}=\Delta\boldsymbol{Q}_{ext}\left(\boldsymbol{\eta}_0,\Delta\boldsymbol{\eta},\Delta\dot{\boldsymbol{\eta}},\boldsymbol{\beta},\boldsymbol{\zeta}\right), \quad (4)$$

which will be used to describe the dynamics of flexible aircraft undergoing arbitrary maneuvers with (not-necessarily small) rigid-body translational and angular velocities, $\boldsymbol{\beta}\in\mathbb{R}^6$, but small elastic deformations, $\Delta\boldsymbol{\eta}\in\mathbb{R}^{6(n_S-1)}$. The damping and stiffness matrices, $\mathcal{C}$ and $\mathcal{K}$, respectively, originate from the perturbation of the discrete gyroscopic and elastic forces of the geometrically nonlinear description and are functions of the instantaneous rigid-body velocities. Together with the mass matrix, $\mathcal{M}$, they account for the coupling between the aircraft structural and rigid-body dynamics. Additional coupling occurs through the aerodynamic loads, which appear in the external forcing term, $\Delta\boldsymbol{Q}_{ext}$. The latter also includes thrust and gravity loads. Quaternions, $\boldsymbol{\zeta}\in\mathbb{R}^4$, are used to describe the instantaneous vehicle orientation and are obtained from the propagation equations of the body-fixed reference frame [43]. Note that Eq. (4) is nonlinear in the rigid-body velocities $\boldsymbol{\beta}$ to allow for arbitrary vehicle maneuvers. The use of quaternions in the parameterization of the vehicle orientation allows for arbitrarily large angles to be represented.

For the efficient representation of the dynamics of the flexible aircraft, we write the perturbation equations, Eq. (4), in terms of the natural modes, $\Phi$, of the unconstrained structure around a geometrically nonlinear trim equilibrium [26]. The resulting modal EOM are written as

$$\Phi^\top\mathcal{M}\Phi(\boldsymbol{\eta}_0)\begin{Bmatrix}\ddot{\boldsymbol{q}}\\ \dot{\boldsymbol{\beta}}\end{Bmatrix}+\Phi^\top\mathcal{C}\Phi(\boldsymbol{\eta}_0,\boldsymbol{\beta})\begin{Bmatrix}\dot{\boldsymbol{q}}\\ \boldsymbol{\beta}\end{Bmatrix}+\Phi^\top\mathcal{K}\Phi(\boldsymbol{\eta}_0,\boldsymbol{\beta})\begin{Bmatrix}\boldsymbol{q}\\ 0\end{Bmatrix}=\Phi^\top\Delta\boldsymbol{Q}_{ext}\left(\boldsymbol{\eta}_0,\boldsymbol{q},\dot{\boldsymbol{q}},\boldsymbol{\beta},\boldsymbol{\zeta}\right), \quad (5)$$

where $\boldsymbol{q}\in\mathbb{R}^{n_\Phi}$ are the corresponding $n_\Phi$ modal coordinates of the truncated system. The projection is limited to small elastic deformations and the resulting modal damping and stiffness matrices, $\Phi^\top\mathcal{C}\Phi$ and $\Phi^\top\mathcal{K}\Phi$, respectively, remain functions of the (large) rigid-body DOF, $\boldsymbol{\beta}$. It is possible however to write these modal matrices in terms of sparse third- and fourth-order tensors. This leads to efficient numerical solutions that keep the nonlinear terms in the rigid-body DOF and all couplings with the linear structure at a low computational cost [38]. The resulting modal EOM are time-marched together with the vehicle propagation EOM using an implicit, constant-acceleration Newmark integration scheme which was modified as in Géradin and Rixen [44] to introduce controlled positive algorithmic damping.

## 2.3 Coupled Aeroelastic and Flight Dynamic Equations

We derive the flexible-aircraft dynamics model by tightly coupling the modal projection of the flexible-body equations in Eq. (5) with the linear UVLM model (1), as shown in Figure 2. Using the modal projection of the structural dynamics, the aerodynamic equations (1) are rewritten as

$$\begin{aligned}\Delta\boldsymbol{\Gamma}^{n+1}&=A_F\Delta\boldsymbol{\Gamma}^n+B_{FS}\Phi\Delta\boldsymbol{u}_\Phi^n+B_{FF}\Delta\boldsymbol{u}_\delta^n+G_{FF}\Delta\boldsymbol{w}_g^n\\ \Delta\boldsymbol{y}_F^n&=\Phi^\top\left(C_F\Delta\boldsymbol{\Gamma}^n+D_{FS}\Phi\Delta\boldsymbol{u}_\Phi^n+D_{FF}\Delta\boldsymbol{u}_\delta^n\right),\end{aligned} \quad (6)$$

where the inputs to the aerodynamic model now include the modal coordinates in the flexible-body equations, $\boldsymbol{q}\in\mathbb{R}^{n_\Phi}$, such that $\boldsymbol{u}_\Phi=\left[\boldsymbol{q}^\top\ \dot{\boldsymbol{q}}^\top\ \boldsymbol{\beta}^\top\right]^\top$. The aerodynamic

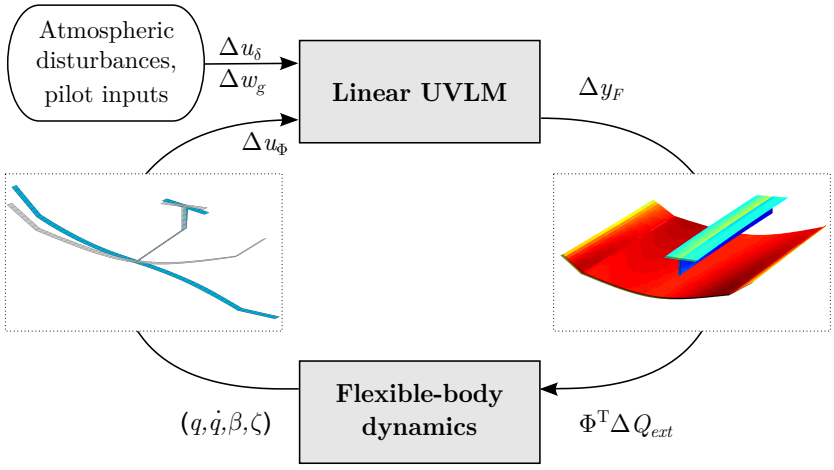



Figure 2: Time-marching solution for maneuvering flexible aircraft.

inputs include the induced disturbance velocities, $\boldsymbol{w}_g \in \mathbb{R}^{3K_b}$, at *each bound aerodynamic panel* and the deployment of $n_\delta$ control surfaces, $\boldsymbol{u}_\delta \in \mathbb{R}^{n_\delta}$. The output vector $\boldsymbol{y}_F \in \mathbb{R}^{n_\Phi+6}$ contains the unsteady loads due to the excitation of the vehicle vibration and six rigid-body modes. Other applied loads, such as thrust and gravity, are accounted for in the flexible-body dynamics subsystem and finally complete the generalized force vector $\Phi^\top \Delta \boldsymbol{Q}_{ext}$ in Figure 2.

Even though we have isolated the linear aerodynamic subsystem, so that it can be independently reduced by balanced truncation [25], the global coupled system equations are still nonlinear.

## 2.4 Modeling Wake Vortex Encounters

The state-space aeroelastic/flight-dynamics formulation, as presented in Section 2.3, provides an effective time-domain tool for fast load calculations of maneuvering flexible aircraft subject to atmospheric disturbances. Following Murua *et al.* [45], atmospheric disturbances such as WVE are modeled in the UVLM as spatially and temporally varying events. As the aircraft travels through the excitation, each collocation point along the aerodynamic surfaces, as defined in Figure 1, experiences a different time-varying gust induced velocity vector. The disturbance input, $\boldsymbol{w}_g$, is used in Eq. (6) to directly account for these gust induced velocities in the current formulation.

### 2.4.1 Wake Vortex Model

We follow the approach described in Kier [18] to model wake vortex encounters, as illustrated in Figure 3. The generating aircraft creates a pair of counter-rotating vortex tubes which are assumed to form parallel to the local airspeed. The initial circulation strength of these wake vortices, $\Gamma_V$, is given by Joukowski's formula at $1g$ steady flight, such that

$$\Gamma_V = \frac{W_G}{\rho V_G b_V}, \tag{7}$$

where $W_G$ is the total weight of the generating aircraft, $V_G$ is its cruise velocity, and $\rho$ is the air density. Once the vortices are generated at the wing tips they move inwards and

the distance between the two vortex lines is generally assumed as

$$b_V = \frac{\pi}{4} b_G, \tag{8}$$

where $b_G$ is the span of the generating aircraft.

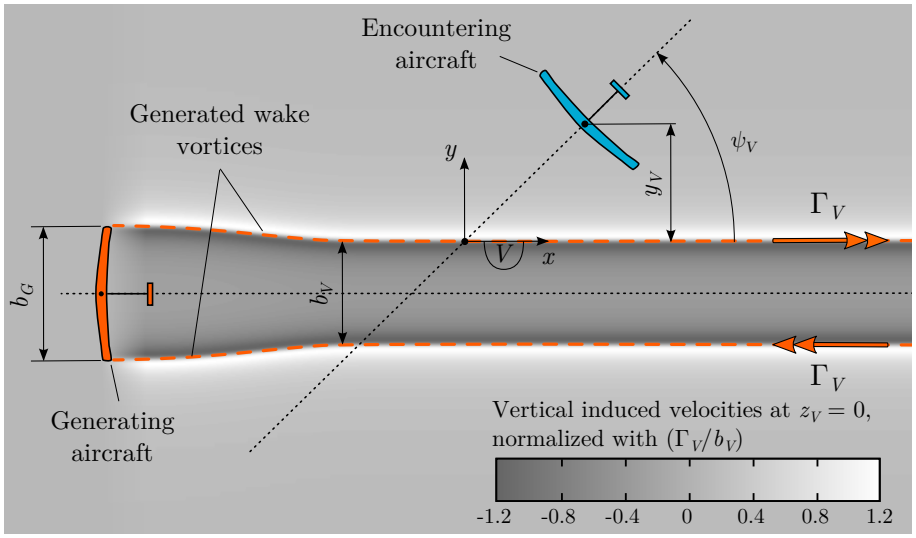



Figure 3: Wake encounter scenario and geometry ($x - y$ plane)

The self-induced velocities of the counter-rotating vortex pair causes the vortices to deform and expand in reality leading to a sinusoidal shape with a growing core vortex radius. Such variations in vortex shape and strength significantly affect the dynamic response of the encountering aircraft which, unlike gust encounter, make it a challenging task to identify critical WVE cases even for one specific generating-encountering aircraft pair. However, perturbations of the wake vortices [13] and the vortex decay [12] were found to alleviate the impact of WVE on the flight dynamic response of rigid aircraft (for the particular problems investigated). This was further demonstrated by Loucel and Crouch [46] in flight simulation studies of an autopiloted passenger aircraft encountering vortices at different stages of the breakup process. To demonstrate the developed load alleviation strategy for a particular example of WVE we make the simplifying assumptions that the wake vortices remain straight with constant core radius, $r_c$, and circulation strength, $\Gamma_V$, i.e. vortex decay is also neglected. Note however that the current formulation can also account for the time-varying effects inherent to the wake vortex propagations and breakup.

### 2.4.2 Wake Vortex Induced Flow Field

The vortex-induced downwash at any point on the encountering aircraft can be obtained using the Biot-Savart law for a vortex line [47], which requires a desingularization at the vortex core. Several models have been proposed to obtain the 2D radial velocity distribution for a completely developed vortex [10, 11, 48, 49]. In this work we implement the commonly used Burnham-Hallock model [10] which identifies the tangential induced velocity distribution in a plane perpendicular to the direction of the wake vortices as

$$V_t(r) = \frac{\Gamma_V}{2\pi} \frac{r}{r_c^2 + r^2}, \tag{9}$$

where $r = \sqrt{y^2 + z^2}$ is the distance from the vortex core to an arbitrary point. Figure 4 shows an example of the induced wake velocity field produced by a generating aircraft with $W_G = 1500$ kg, $V_G = 30$ m/s, $b_G = 30$ m, $\rho = 0.0889$ kg/m$^3$. Figure 3 also illustrates the vertical component of the velocity distribution at $z = 0$, i.e. in the plane of the generating aircraft.

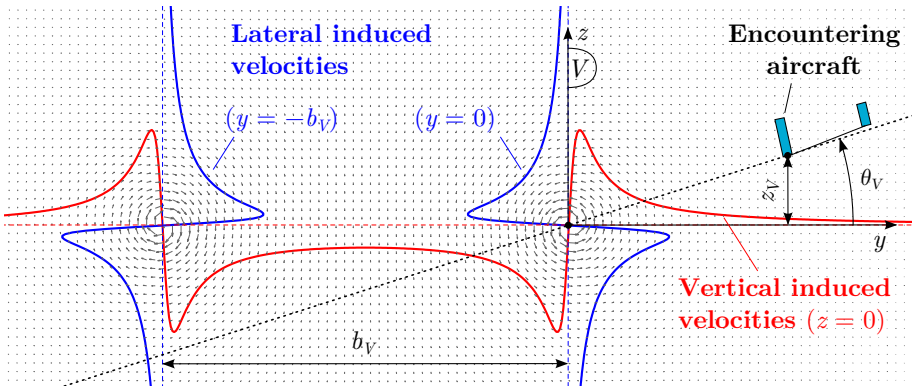



Figure 4: Wake encounter geometry with induced velocity field in $y-z$ plane for encounter angles $\psi_V = 90$ deg and $\theta_V$.

The vortex core radius, $r_c$, significantly affects the peak velocities in the flow field, as highlighted by the superimposed lateral and vertical velocity components in Figure 4. A radius of 2% of the aircraft wing span was chosen in this work which is within the 1-5% range that has been identified in experimental flight tests [15, 18]. Note that the tangential velocities are computed in the vortex frame of reference, $V$, where the origin of the $V$ frame is placed in the center of the starboard wake vortex, as defined in Figures 3-4.

### 2.4.3 Parameterization of Wake Vortex Encounters

To explore different encounter scenarios in this work we parameterize the encounter geometry using the relative position $(y_V, z_V)$ and orientation between the body-attached frame, $A$, of the encountering aircraft and the vortex frame, $V$. The latter is parametrized in this work using Euler angles $(\phi_V, \theta_V, \psi_V)$, where $\psi_V$ and $\theta_V$ are the yaw and pitch encounter angles, as defined in Figures 3-4. To obtain the vortex-induced downwash acting on the aircraft, i.e. the disturbance $\boldsymbol{w}_g$ to the aerodynamic model in Eq. (6), the induced velocities are transformed to the body-fixed frame of the encountering aircraft.

# 3 Control System Design

In this work $\mathcal{H}_\infty$ control synthesis is used for the efficient design of WVE load alleviation systems with multiple inputs and outputs. A similar approach was found previously[27] to perform very well in load alleviation in discrete gust responses. For this purpose we first linearize the rigid-body DOF to arrive at a monolithic description of the flexible-aircraft dynamics (Section 3.1). The model order of the resulting system, however, is too large for direct control synthesis and this is tackled by a model reduction approach that has been previously demonstrated on similar aeroelastic systems [25]. The resulting control model finally provides the basis for a 2-DOF feedforward and feedback control scheme using $\mathcal{H}_\infty$ control (Section 3.2).

## 3.1 Linearized Control Model

As the linear UVLM in Eq. (1) is written in discrete time, a temporal discretization of the flexible-body system, defined now by the linearization of Eq. (5), is also required before the fluid/structure coupling. Using a standard Newmark-$\beta$ discretization this leads to a linear aeroelastic state-space system [22]

$$\begin{aligned} \Delta \boldsymbol{x}^{n+1} &= A\Delta \boldsymbol{x}^{n} + G\Delta \boldsymbol{w}_g^{n} + B\Delta \boldsymbol{u}_\delta^{n} \\ \Delta \boldsymbol{y}^{n} &= C\Delta \boldsymbol{x}^{n}, \end{aligned} \tag{10}$$

where the state vector that completely determines the system dynamics is

$$\boldsymbol{x} = \left[\boldsymbol{\Gamma}_b^\top \ \boldsymbol{\Gamma}_w^\top \ \dot{\boldsymbol{\Gamma}}_b^\top \mid \boldsymbol{q}^\top \ \dot{\boldsymbol{q}}^\top \ \ \boldsymbol{\beta}^\top \ \boldsymbol{\Theta}^\top\right]^\top. \tag{11}$$

The orientation of the aircraft is now given in terms of the Euler angles, $\boldsymbol{\Theta} \in \mathbb{R}^3$, instead of the quaternion parameterization in Eq. (5). This firstly simplifies the linearization, as quaternions introduce nonlinear algebraic constraints, and ensures that the closed-loop system is strictly Hurwitz [27]. The latter is required for $\mathcal{H}_\infty$ control synthesis which will be addressed in the next subsections. The (aerodynamic) inputs to the system account for arbitrary gust distributions, $\boldsymbol{w}_g$, and deflections of the control surfaces, $\boldsymbol{u}_\delta$, in a (closed-loop) time-marching solution. The output vector of the LTI system, $\boldsymbol{y}$, can include aerodynamic loads, elastic deformations, aircraft position, attitude, etc. The focus of this work is on load alleviation where we measure and regulate the wing root strains unless otherwise stated.

The relatively-large model order of the linearized control system of $\mathcal{O}(10^4)$ prevents its use in the efficient design of robust controllers. Following the model reduction approach recently demonstrated by the authors [25] for aeroelastic systems, we will use balanced realization [50, 51] to obtain a similarity transformation $\mathcal{T}$ that balances and ranks the stable system $\{A, (G, B), C\}$, such that each balanced state $\hat{\boldsymbol{x}} = \mathcal{T}\boldsymbol{x}$ is equally controllable and observable. The state-space representation of the resulting balanced control model is then given by

$$\begin{aligned} \Delta \hat{\boldsymbol{x}}^{n+1} &= \mathcal{T}A\mathcal{T}^{-1}\Delta \hat{\boldsymbol{x}}^{n} + \mathcal{T}G\Delta \boldsymbol{w}_g^{n} + \mathcal{T}B\Delta \boldsymbol{u}_\delta^{n} \\ \Delta \boldsymbol{y}^{n} &= C\mathcal{T}^{-1}\Delta \hat{\boldsymbol{x}}^{n}, \end{aligned} \tag{12}$$

which can be reduced by truncating balanced states that contribute little to the transmission path between the system inputs (disturbances and control surface inputs) and outputs (root strains). The resulting reduced-order system, typically of $\mathcal{O}(10^2)$, is denoted as $H = \left\{\hat{A}, (\hat{G}, \hat{B}), \hat{C}\right\}$ in this work and accounts for the coupling effects between the aircraft 3D aero-, structural, and flight dynamics. Details on the model reduction approach and the numerical schemes used for balancing large aeroelastic systems have been discussed in a previous paper [25].

## 3.2 Dynamic Load Alleviation Strategy

We will follow the 2-DOF control strategy of Figure 5, which complements a linear feedback controller, $K$, with an optional feedforward controller, $F$. Both controllers are designed to use conventional control surfaces to reduce aircraft loads, with the commands of the feedforward controller being simply added to the control surface inputs of the

feedback control system. The resulting control surface inputs, $\boldsymbol{u}_\delta$, are then commanded to the (nonlinear) flight simulation plant, Eq. (6), to investigate the 2-DOF controller performance for possibly asymmetric WVE and nonlinear flight dynamics.

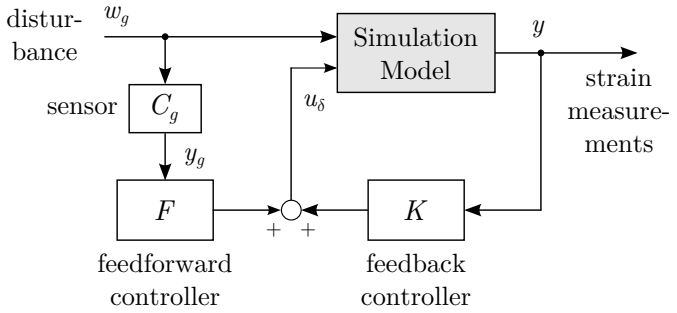



Figure 5: 2-DOF system for feedforward and feedback control.

Feedforward schemes have the advantage that direct measurements of the flow can be used to compensate for the disturbance before the aircraft dynamics is affected [9, 32, 35]. However, since a feedforward system cannot reject all gust excitations perfectly, due to control surface constraints, sensor limitations, actuator dynamics or model mismatch [9], a feedback controller, $K$, is included to suppress possible residual structural excitations. Hence, for the feedback control loop strain measures at the wing roots suffice. The feedforward control system on the contrary requires direct measurements of the flow, which will be addressed in more detail in Section 3.2.1. Hence, the feedforward controller is only active when a disturbance is detected and therefore has no impact on the vehicle stability characteristics.

### 3.2.1 Disturbance Measurement

Direct measurement of the disturbances is crucial in the design of a feedforward control system for load alleviation. Assuming that the aircraft dimensions are small compared to typical gust size, measurement of the instantaneous vertical component of the airspeed at a few discrete points on the vehicle is adequate to determine the flow field for disturbance rejection [9]. More measurement points can be added along the wing span for very large aircraft or for vehicles with unconventional geometries.

It will be assumed that measurements of the vertical gust component at discrete points is obtained using 5-hole probes (5HP) [9, 52]. These devices measure the local wind vector which, if coupled with a GPS receiver to measure the aircraft inertial velocity components, provide the instantaneous angle of attack changes or the vertical gust velocities. In the proposed 2-DOF control scheme in Figure 5, these discrete velocity measurements, $\boldsymbol{y}_g$, are modeled as

$$\boldsymbol{y}_g = C_g \boldsymbol{w}_g, \tag{13}$$

where $\boldsymbol{w}_g$ include all three components of the velocity disturbance at each collocation point of the aerodynamic panels and the operator $C_g$ is used to identify the collocations points where the different components of the 3D disturbance are measured. These direct measurements are used in this work to drive the feedforward controller for dynamic load alleviation.

### 3.2.2 Two-Degree-Of-Freedom Control Synthesis

In the absence of model uncertainties the design of the feedback controller $K$ and the feedforward controller $F$ introduced in Figure 5 can be separated [53]. Due to possible model mismatch and to facilitate the synthesis of a multivariable feedback and feedforward controller we will focus on the joint synthesis of $K_\infty = [K \;\; F]$, such that

$$\boldsymbol{u}_\delta = K_\infty \begin{bmatrix} \boldsymbol{y}_g \\ \boldsymbol{y} \end{bmatrix}. \tag{14}$$

In this work we use $\mathcal{H}_\infty$ control synthesis to synthesize a controller $K_\infty$ that minimizes the wing loads of the aircraft, $\boldsymbol{y}$, subject to the external disturbances $\boldsymbol{w}_g$ measured at discrete points $\boldsymbol{y}_g$. The output of the controller are the control surface deflections $\boldsymbol{u}_\delta$. Following the extension in Limebeer *et al.* [54], we design a 2-DOF $\mathcal{H}_\infty$ controller in a single step which includes a feedthrough of the system disturbances for the feedforward control part.

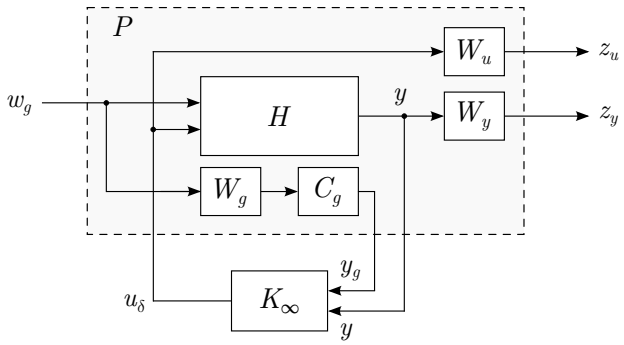



Figure 6: Augmented plant for 2-DOF $\mathcal{H}_\infty$ control design.

The resulting control problem is illustrated in Figure 6 where $H$ corresponds to the linearized reduced-order control model defined in Eq. (12). The weighting matrices $W_y$ and $W_u$ are introduced to tune the controller for maximum control performance subject to control surface constraints, and $\boldsymbol{z}_y$ and $\boldsymbol{z}_u$ are the corresponding weighted output and input signals, respectively. The disturbance measurement at discrete points, $\boldsymbol{y}_g$, as defined in Eq. (13), and the strain measures, $\boldsymbol{y}$, form the outputs of the augmented plant $P$. The weighting matrix $W_g$ has been introduced in the feedthrough to tune the feedforward controller. An alternative approach would be to scale the feedforward path after the synthesis but an integrated one-step control design approach was preferred in this work. This leads to a mixed-sensitivity $\mathcal{H}_\infty$ control problem to improve the disturbance rejection assuming perfect measurements [53]. Finally, as the frequency range of the disturbance in a WVE scenario were found to vary substantially depending on the specific conditions of the encounter, we ignore information on the shape and frequency of the disturbance in the design of the controller in this exploratory exercise. However, some knowledge of the inherent system dynamics could be considered in further iterations of the methodology, which could further improve the control performance.

The 2-DOF design problem can be cast as a general $\mathcal{H}_\infty$ optimization problem to find stabilizing controllers $K_\infty$ that minimize the $\mathcal{H}_\infty$ norm of the the closed-loop transfer function from $\boldsymbol{w}_g$ to $\boldsymbol{z} = [\boldsymbol{z}_y \;\; \boldsymbol{z}_u]^\top$ given by the linear fractional transformation $\boldsymbol{z} = F_l(P, K_\infty)\boldsymbol{w}_g$ [53]. The corresponding state-space representation of the augmented system,

$P$, can therefore be written as

$$\begin{bmatrix} \Delta\hat{\boldsymbol{x}}^{n+1} \\ \Delta\boldsymbol{z}_y^n \\ \Delta\boldsymbol{z}_u^n \\ \Delta\boldsymbol{y}^n \\ \Delta\boldsymbol{y}_g^n \end{bmatrix} = \underbrace{\left[\begin{array}{c|cc} \hat{A} & \hat{G} & \hat{B} \\ \hline W_y\hat{C} & 0 & 0 \\ 0 & 0 & W_u \\ \hline \hat{C} & 0 & 0 \\ 0 & W_gC_g & 0 \end{array}\right]}_{P} \begin{bmatrix} \Delta\hat{\boldsymbol{x}}^n \\ \Delta\boldsymbol{w}_g^n \\ \Delta\boldsymbol{u}_\delta^n \end{bmatrix}. \tag{15}$$

where $P$ has been constructed as a discrete-time system from the discrete-time control model. Further conversion to continuous time is required for the subsequent control synthesis. This is done using zero-order hold.

The Robust Control Toolbox [55] in Matlab® is finally used to solve the $\mathcal{H}_\infty$ problem based on two Riccati solutions [56]. Due to the still comparatively large size of the reduced-order control model in Eq. (12) of $\mathcal{O}(10^2)$, a suboptimal $\mathcal{H}_\infty$ control problem is solved efficiently by finding all stabilizing controllers $K_\infty$ that suffice [53]

$$||F_l(P, K_\infty)||_\infty < \gamma, \tag{16}$$

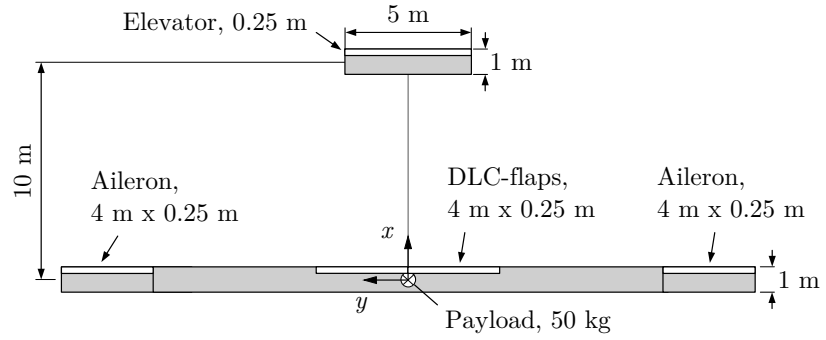
with $\gamma = 0.01$ throughout this work. Details on the algorithm can be found in section 9.3.4 of Skogestad and Postlethwaite [53]. Note that the resulting controller is of the same order as the underlying reduced-order control model and no further model reduction of synthesized controller was explored in this work.

# 4 Numerical Studies

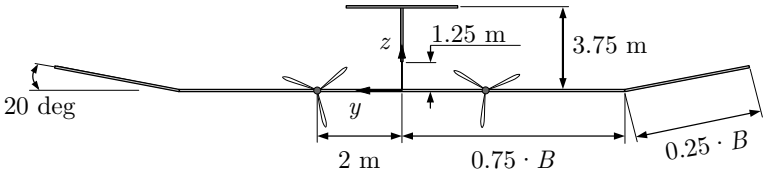
A representative HALE aircraft configuration has been modeled in our in-house solver `SHARP` and will be used to demonstrate the present approach for WVE simulation and investigate the potential for load alleviation. The various modules in `SHARP` have been verified for this same platform in previous publications [22, 25, 26, 37, 38, 57]. The characteristics of the vehicle will be briefly defined in Subsection 4.1. The aeroelastic/flight-dynamic simulation model is then exercised in Section 4.2 to explore the effect of wake vortex strength, different encounter angles and displacement on the vehicle flight dynamic response. For the critical encounter case, we finally present different load alleviation strategies in Section 4.3 using direct forward disturbance measurements and dedicated control surfaces.

## 4.1 Vehicle geometry and reference conditions

The flexible aircraft configuration used for the numerical studies in this work is shown in Figure 7. This vehicle was introduced in a previous work [25, 26] and it was purposely defined by a very small number of parameters to allow easy reproducibility of the results. Its geometry and material properties are shown again in Table 1 for completeness. The aircraft consists of a large-aspect-ratio flexible wing and rigid fuselage and T-tail. It is powered by two massless propellers, which are modeled as point forces rigidly linked to the main wing. The total mass of the aircraft, including payload and structural mass, is 75.4 kg. The geometry also illustrates the control surfaces used in this work for actuation in abrupt WVE [9].




(a) Top view




(b) Front view

Figure 7: Undeformed HALE aircraft geometry.

The flexible vehicle is trimmed at a free-stream velocity of $V_\infty = 30$ m/s and an altitude of 20 km (air density $\rho = 0.0889$ kg/m$^3$) to obtain the geometrically-nonlinear, deformed configuration at steady level flight. A converged trim solution was obtained using 8 bound aerodynamic panels chordwise and 2 panels per spanwise meter of lifting surfaces [26]. A wake length of 20 m and a time step of $dt = 5 \times 10^{-3}$ s was required to resolve the possibly fast dynamics in WVE, leading to 9846 aeroelastic states (8769 aerodynamic, 1068 structural and 9 rigid-body dynamic states) in the subsequent transient analyses.

During nominal operating conditions the vehicle exhibits wing tip deflections of 13% compared to the semi span of the main wing, $B = 16$ m. The resulting large effective wing dihedral at steady state has a significant effect on the stability characteristics of the vehicle [26], which is evident in Table 2 comparing the (flexible) flight dynamics modes of the flexible configuration to the rigid aircraft modes. The vehicle stability characteristics are obtained directly from an eigenvalue analysis of the monolithic system in Eq. (10), which provides the flight dynamic, aeroelastic, and aerodynamic modes of the flexible aircraft. Note in particular the effect of flexibility on the lightly-damped phugoid and spiral modes. The first symmetric and antisymmetric aeroelastic modes have also been included. The antisymmetric coupled mode is particularly lightly damped, which will be relevant for the subsequent open-loop studies of WVE.

## 4.2 Open-Loop Studies: Effect of WVE on Aircraft Dynamics

We first explore the effect of WVE on the flight dynamic response of the flexible vehicle. The geometry of the wake vortex generating aircraft and the flight path of the encountering aircraft through the resulting disturbance field, as defined in Figures 3 and 4, will clearly affect the vehicle response. Hence, the following parameters are used next to fully describe WVE scenarios: vortex strength ($\Gamma_V$), distance between port and starboard vortex ($b_V$), and position ($y_V, z_V$) and orientation ($\phi_V, \theta_V, \psi_V$) of the encountering aircraft with respect

Table 1: HALE aircraft properties. [26]

| | Main wing | Tail plane |
|---|---|---|
| Chord, $c$ | 1 m | 0.5 m |
| Semi-span, $B$ | 16 m | 2.5 m |
| Elastic axis (from l.e.) | 0.5 m | 0.25 m |
| Center of gravity (from l.e.) | 0.5 m | 0.25 m |
| Mass per unit length | 0.75 kg/m | 0.08 kg/m |
| Moment of inertia | 0.1 kg·m | 0.01 kg·m |
| Torsional stiffness | $2\times10^4$ N·m$^2$ | $\infty$ |
| Bending stiffness | $4\times10^4$ N·m$^2$ | $\infty$ |
| In-plane bending stiffness | $8\times10^6$ N·m$^2$ | $\infty$ |

Table 2: Stability characteristics of the HALE aircraft at trimmed flight.

| | | Flexible [Hz] | | Rigid [Hz] | |
|---|---|---|---|---|---|
| Mode | Symm. | Freq. | Damp. | Freq. | Damp. |
| Phugoid | S | 0.048 | $8 \times 10^{-4}$ | 0.043 | $2 \times 10^{-3}$ |
| Spiral | A | - | 0.014 | - | $3 \times 10^{-3}$ |
| Dutch roll | A | 0.202 | 0.314 | 0.207 | 0.059 |
| Short period | S | 0.258 | 0.373 | 0.150 | 0.853 |
| 1$^{\text{st}}$ Aeroelastic | S | 0.763 | 0.951 | - | - |
| 2$^{\text{nd}}$ Aeroelastic | A | 3.427 | 0.139 | - | - |

to the wake frame of reference, $V$. The parameter space to determine the critical loads due to WVE becomes therefore quite large and requires a large number of simulations to compute the load envelope for a given vehicle configuration. In this work, we will restrict ourselves to the variations of the encounter angle, $\psi_V$, and vertical offset, $z_V$.

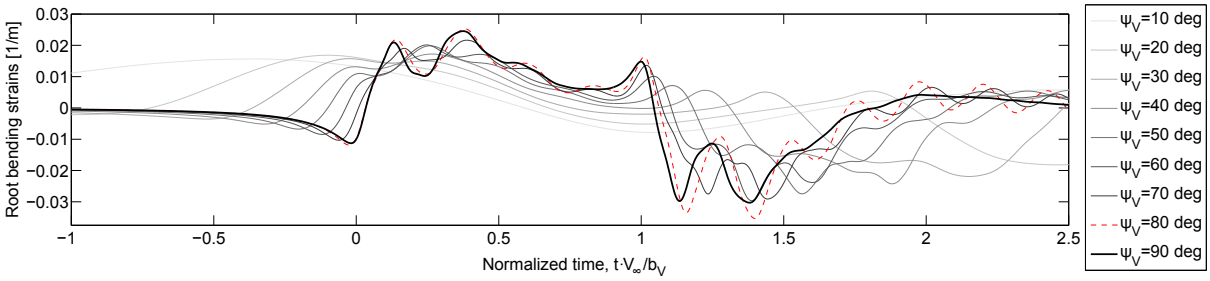
We will investigate the encounter of the lightweight vehicle defined above with a heavier vehicle ($W_G = 2800$ kg, $b_G = 50$ m, $V_G = 8$ m/s, typical of the NASA Helios prototype). As it will be seen, the vortex strength of $\Gamma_V = 100$ m$^2$/s of the resulting wake vortices, with a distance of $b_V = 39.3$ m, will lead to encounter loads at the wing root of the lighter UAV that are comparable to those in discrete gust encounters as required for FAR Part 25 certification [58] and demonstrated in previous work by the authors [25].

### 4.2.1 Effect of Encounter Angle on WVE

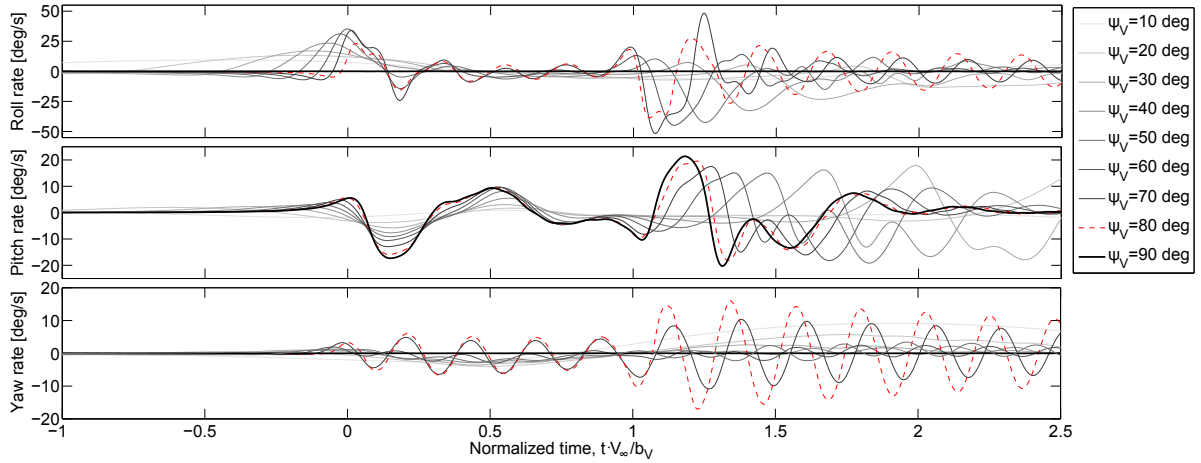
For conventional (rigid) transport aircraft, the most hazardous WVE scenario is usually given by an encountering aircraft in landing approach ($\phi_V = 0, \theta_V, \psi_V = 0$) where the induced rolling moments can lead to large roll excursions [2, 9, 17]. However, recent flight tests and numerical simulations have demonstrated that critical WVE loads may occur at

encounter angles $45 \leq \psi_V \leq 90$ deg ($\phi_V = 0, \theta_V = 0$) [16, 18, 19, 21]. These findings are confirmed in Figure 8(a), which presents the effect of varying the encounter angle, $\psi_V$, on the bending loads at the root of the starboard main wing. Note that in this work we investigate wing loads in terms of the root bending and torsion strains which are obtained in the current beam formulation from the moment curvatures at the wing root.

The time histories of the WVE are normalized in this work with the flight speed of the encountering aircraft, $V_\infty$, and the distance $b_V$ to emphasize potential encounter events at $tV_\infty/b_V = \{0, 1\}$. The wake vortices are modeled however as 3D spatial disturbances which can affect the flight dynamic response of the encountering aircraft. This is illustrated in Figure 8(b) which shows the impact of the WVE on the aircraft attitude rates for different encounter angles, $\psi_V$, where the aircraft orientation with respect to the $V$ frame is given here in terms of Euler angles.




(a) Bending strains at root of starboard main wing

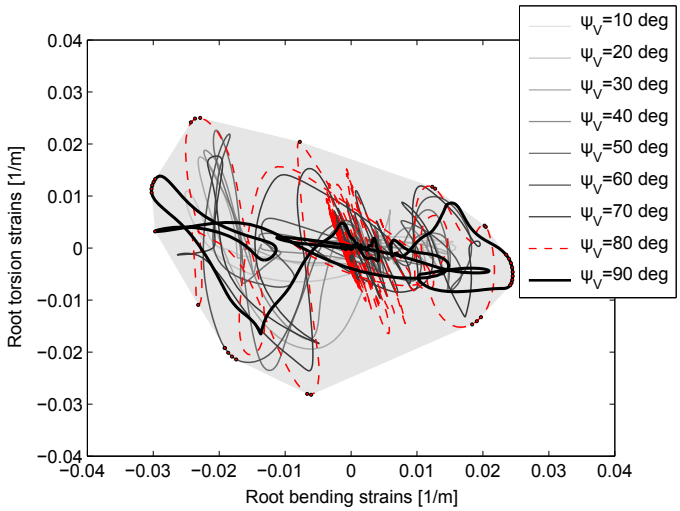



(b) Attitude rates of encountering aircraft

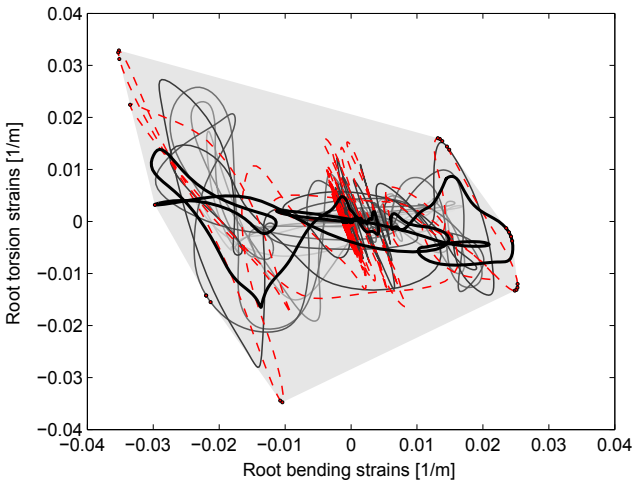
Figure 8: Wing loads and aircraft orientation against encounter angle $\psi_V$. The maximum loads appear for $\psi_V = 80$ deg. [$z_V = 0.5$ m, $\theta_V = 0$]

Hence, for encounter angles of $\psi_V < 90$ deg the flexible aircraft suffers significant roll and yaw excursions due to the induced rolling moments. For $40 < \psi_V < 90$ deg the asymmetric disturbance excites the lightly-damped antisymmetric aeroelastic mode at 3.43 Hz, as defined in Table 2. This is particularly obvious for $\psi_V = 80$ deg with persistent roll and yaw oscillations present even long after the WVE which demonstrates the significant interaction between the vehicle structural and flight dynamics. In fact, this aeroelastic interaction not only produces the maximum root bending moments for $\psi_V = 80$ deg, but also leads to large roll perturbations after the encounter with the second wake vortex due to the dynamic excitation of the structure. The latter highlights

the importance of an integrated aeroelastic modeling approach in the design of more efficient aircraft and the need for a nonlinear flight dynamics model, as introduced in the simulation plant in Section 2.3.




(a) At root of port main wing




(b) At root of starboard main wing

Figure 9: Envelope of bending vs. torsion strains for varying encounter angles, $\psi_V$. $[z_V = 0,\ \theta_V = 0]$

As seen above, variation of the encounter angle leads to asymmetric disturbances acting on the aircraft. For a comprehensive load analysis, Figure 9 compares the torsion and bending loads at the roots of the port and starboard wings for varying encounter angles, $\psi_V$. The convex hull is obtained from the different load cases of the encounter angle study. The resulting load envelope diagrams are superimposed in Figure 9 and demonstrate that the asymmetric excitations cause significantly higher loads on the starboard wing due to the vehicle flight dynamic response. In fact, for the present sweep study maximum loads in bending and torsion occur on the starboard wing for $\psi_V = 80$ deg.

### 4.2.2 Effect of Vertical Offset on WVE

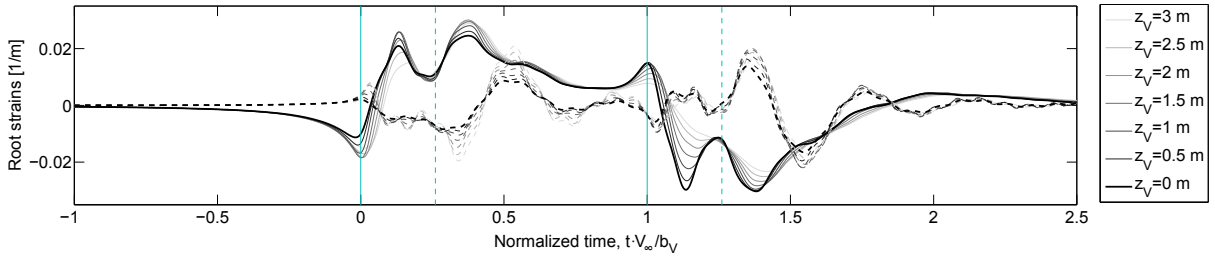
To investigate the aircraft response to WVE in detail, we further vary the vertical offset, $z_V$, between the origin of frame $A$ attached to the initial center of gravity of the encountering aircraft and the origin of the vortex frame, $V$. The encountering aircraft is assumed to approach the wake vortices on a perpendicular flightpath, i.e. $\psi_V = 90$ deg and $\phi_V, \theta_V = 0$. As the HTP is raised by 3.75 m with respect to the origin of the $A$ frame, as defined in Figure 7, we can expect a significant impact of vertical offset, $z_V$, on the flexible aircraft response.

Figure 10(a) shows the root bending (solid curves) and torsion (dashed curves) strains of the starboard main wing for different vertical offsets. The encounter events at $tV_\infty/b_V = \{0, 1\}$ are highlighted in Figure 10 with vertical lines, where the solid lines indicate encounter events of the leading edge of the main wing and the dashed lines the corresponding events for the HTP. To investigate the effect of the vertical offset, $z_V$, Figure 10(b) shows the induced vertical velocities at the root of the main wing (solid curves) and the HTP (dashed curves) for the different cases. As the flightpath is not prescribed in this work, the resulting flight dynamic response causes the vehicle altitude to deviate from the initial defined vertical offset. This is illustrated in Figure 10(c) which shows the (tangent) velocity field induced by both wake vortices and the resulting flightpath of the main wing (solid curves) and the HTP (dashed curves) in the $y - z$ plane of frame $V$. Note that $z_V$ has been normalized with the vortex spacing $b_V$.

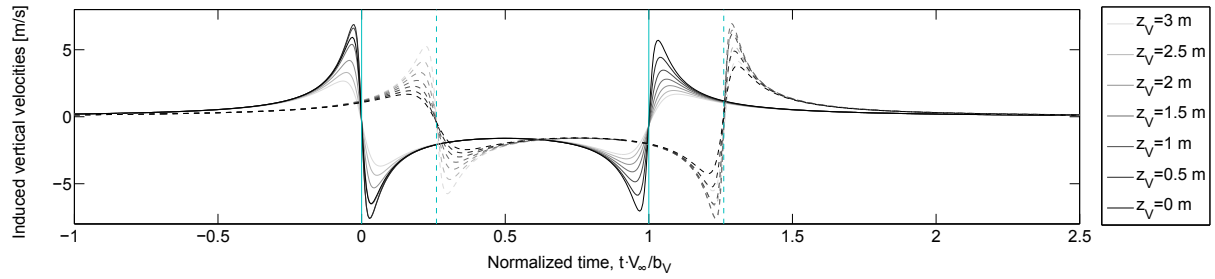
The dynamic loads on the main wing are clearly affected by the vicinity of the lifting surfaces to the wake vortices but also the subsequent dynamic response of the vehicle. A slight change of altitude can substantially change the peak loads that occur at each vortex encounter. The maximum peak loads at the first vortex encounter ($tV_\infty/b_V = 0$) occur for $z_V = 3$ m after the HTP passes the source of the first vortex. The abrupt change of induced velocities on the HTP leads to high pitch rates (not shown here), which in return cause large deflections of the main wing. The encounter with the second vortex ($tV_\infty/b_V = 1$), however, is dominated by the vicinity of the main wing to the vortex source and the dynamic excitations that remain from the first encounter. This finally leads to maximum root bending loads for $z_V = 0$. The torsion strains on the other hand appear to be dominated by the distance between the HTP and the vortices, and the maximum torsion loads appear for $z_V = 3$ m (see Figure 10(a)).

## 4.3 Closed-Loop Studies: Load Allevation in WVE

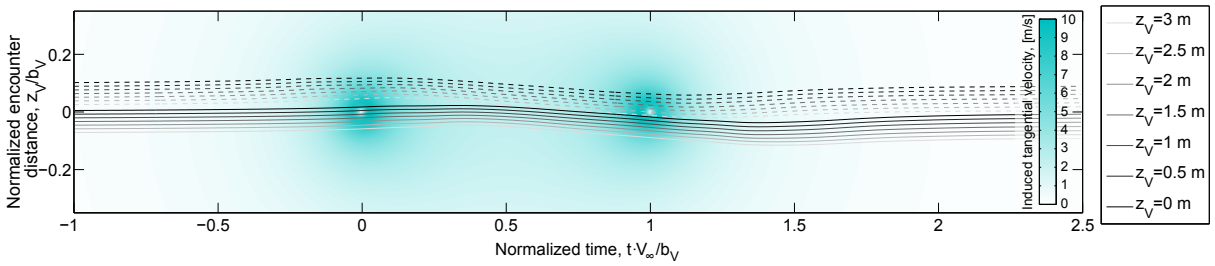
The open-loop studies in Section 4.2 suggest that an effective WVE load alleviation system design should include information about the vehicle flight dynamic response and the fast wake vortex excitations. Hence, in this section we will investigate four different strategies using disturbance measurements (e.g. 5-hole probes (5HP)), and direct lift control (DLC) flaps, as defined in Figure 7. The different sensor and actuator configurations are outlined in Table 3, where the controller for each configuration is synthesized using the 2-DOF approach described in Section 3.2.2. The weightings in the control synthesis are derived for the head-on encounter case ($\psi_V = 90$ deg) with equal weighting on outputs, $W_y = \text{diag}(50\ 50\ 50\ 50)$, to regulate both bending and torsion strains at the root of the left and right wings. Note that no importance is given here to the vehicle velocities or maintaining a defined trajectory. For the cases without disturbance measurements (*Conv, DLC*) the disturbance feedthrough term, $\Delta \boldsymbol{y}_g^n = W_g C_g \Delta \boldsymbol{w}_g^n$, in the definition of the augmented system in Eq. (15) will be neglected. The configuration *Conv* has been included here to




(a) Bending (solid) and torsion (dashed) strains at root of main wing




(b) Induced vertical velocities at root of main wing (solid) and HTP (dashed)




(c) Flightpath of main wing (solid) and HTP (dashed) through wake vortices with induced 2D tangential velocity field superimposed

Figure 10: Effect of vertical offset, $z_V$, on WVE. [$\theta_V = 0$, $\psi_V = 90$ deg]

consider conventional controllers based on existing control surfaces (ailerons and elevator). Note that the vehicle thrust from the propellers remains constant in the simulations.

To justify the use of DLC flaps for load alleviation in addition to ailerons, Figure 11 shows the Bode magnitude plots of the linearized (full-order) control model in Eq. (10) from the starboard DLC flap, aileron, and the elevator to the starboard root torsion and bending strains of the main wing. The stability characteristics of the HALE aircraft, as presented in Table 2, are also reflected in the Bode magnitude plots where the lightly-damped Phugoid mode at 0.048 Hz leads to dominant bending strains in Figure 11(b). In addition to the flight dynamic modes, the torsional response in Figure 11(a) is also affected by the higher frequency aeroelastic torsion modes above 9 Hz. Since the DLC flaps are located close to the root of the main wing, they are not as vulnerable to aeroelastic effects as the ailerons and are therefore more effective in the control of the dominant flight dynamic modes. Deflection of the ailerons on the other hand leads to coupled bending/torsion deformations which makes the ailerons more suitable to control the aeroelastic modes which can also be excited in WVE. Finally, the elevator has to go through relatively slow aircraft pitch responses to alleviate loads on the main wing which may be too slow to be effective in WVE.

Table 3: Definition of sensor and actuator configurations for load alleviation with corresponding input weights for $W_y = \text{diag}(50\ 50\ 50\ 50)$.

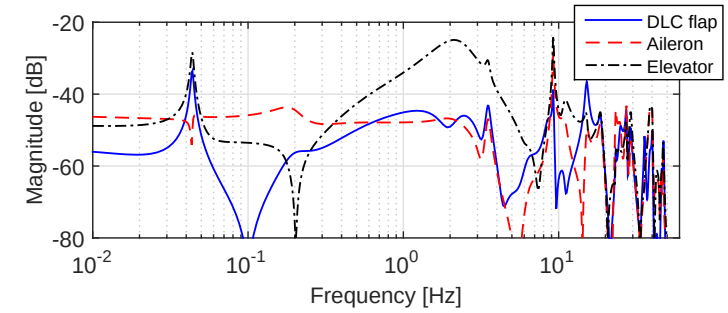
| | | $W_u$ | | $W_g$ |
|---|---|---|---|---|
| Strategy | DLC flaps | ailerons | elevator | 5-hole-probe |
| *Conv* | 0 | 2.25 | 0.75 | - |
| *5HP* | 0 | 2.50 | 1.75 | $2 \times 10^{-3}$ |
| *DLC* | 1.25 | 2.00 | 0.75 | - |
| *DLC&5HP* | 1.25 | 1.50 | 1.50 | $2 \times 10^{-3}$ |

### 4.3.1 Controller Design

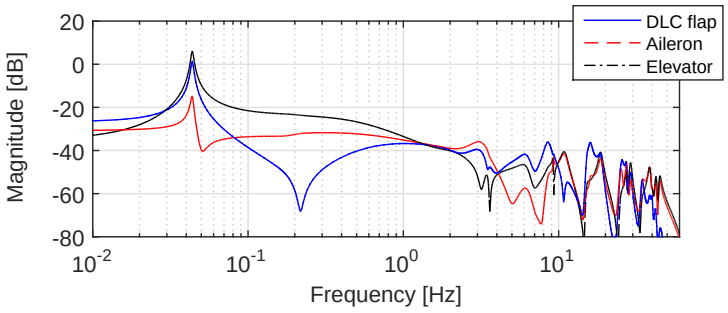
Following the approach outlined in Section 3.1, and discussed in detail in a previous work [25], the full-order control system with 9846 aeroelastic, aerodynamic, and flight dynamic states is reduced to enable $\mathcal{H}_\infty$ control synthesis for WVE load alleviation. Based on the system Hankel singular values of the balanced control system (not shown here), we consider four different control systems with 60, 100, 140, and 200 states. Figure 12 compares the structural response of the selected reduced-order systems by tracking the wing root bending strains in a head-on encounter ($z_V = 0$, $\theta_V = 0$, and $\psi_V = 90$ deg). They are compared to the the full-order (linear) control model and the (nonlinear) simulation plant. The differences between the full-order control and simulation system responses become larger after the second encounter ($tV_\infty/b_V \geq 1$). In the control system response the disturbance field is prescribed, which highlights the importance of accounting for the flight dynamics of the encountering aircraft in WVE simulations. Comparing the different reduced-order control systems, the 100-state control model accurately predicts the encounter loads in bending and torsion (not shown here for brevity) for prescribed disturbance velocities and will be used for the subsequent control synthesis. This leads to a dynamic controller of the same size as the reduced-order control model.

To simplify the control problem in this work, we focus on regulating the strains at the root of the main wing only, but the approach could also include loads at the HTP or the vehicle velocities for trajectory control. The objective in this work is to minimize both root bending and torsion strains, which was found to provide the best balance to alleviate loads due to the combined effect of aerodynamic excitation and the resulting vehicle dynamics. The latter is best addressed by controlling the wing twisting, which is seen to dampen the first antisymmetric aeroelastic mode. As demonstrated in the open-loop studies in Section 4.2.1, this lightly-damped mode leads to the larger loads in asymmetric encounter scenarios.

The improved performance of a combined bending and torsion controller for this particular vehicle configuration is also demonstrated in Figure 13, which shows a zoom of the root loci of the closed-loop aeroelastic systems obtained by minimizing (a) bending only and (b) bending and torsion strains. Both closed-loop systems were obtained using a conventional (*Conv*) controller with the weights defined in Table 3 and setting $W_y = \text{diag}(0\ 50\ 0\ 50)$ for bending only and $W_y = \text{diag}(50\ 50\ 50\ 50)$ to regulate both bending and torsion strains. Comparison to the open-loop stability characteristics shows that the combined controller does a much better job in stabilizing the antisymmetric




(a) Root torsion strains




(b) Root bending strains

Figure 11: Bode magnitude plot from control surface inputs to strains at the starboard main wing.

aeroelastic mode but also improves the flight dynamic stability characteristics.

An important aspect, which is not considered in this work, are limitations of the control performance due to delays and other sensor issues such as drift and noise. Especially the effect of delay from estimation or sensing can be critical in the practical implementation of the proposed controller due to the possibly fast dynamics of WVE. In the next subsections however we will assume ideal conditions without sensor delay, bias and noise to demonstrate the aeroelastic modeling approach for load alleviation.

### 4.3.2 Closed-Loop Response to Head-on Encounters

The different $\mathcal{H}_\infty$ controllers are synthesized for a head-on case with $\theta_V = 0$, $\psi_V = 90$ deg, and $z_V = 0$. The weights on the controller inputs (DLC, ailerons, or elevator) and the strain outputs, as defined in Table 3, are tuned to ensure maximum control surface deflections below $\pm 10$ deg for this configuration. Note that we chose the same weights, $W_y = 50$, for bending and torsion strains.

The performance of the different controllers is demonstrated in Figure 14 which shows the closed-loop responses for the WVE head-on encounter scenario with $z_V = 0$. Note that the results in Figure 14 are obtained using the same reduced-order control system as previously used for the control synthesis and tuning. To compare the closed-loop performance of the different controllers we focus on the bending strains at the root of the starboard main wing in Figure 14(a). Figure 14(b) shows the corresponding control surface deflections (starboard DLC flaps and aileron) which are saturated when the constraints are exceeded.

The comparison with the open-loop response shows that, what we have called the

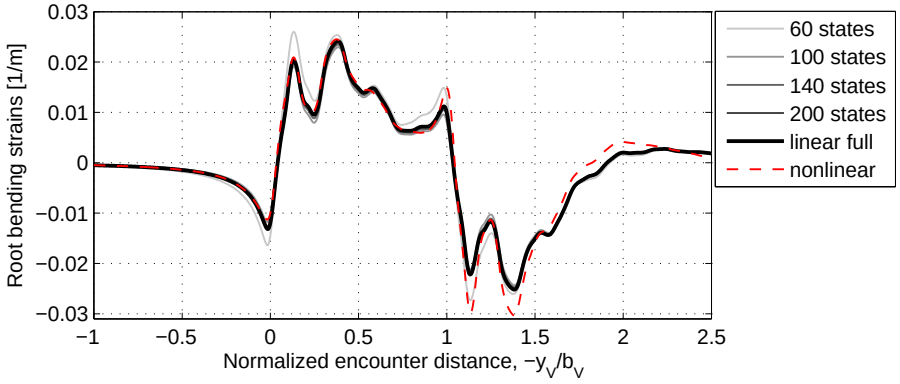



Figure 12: Comparison of reduced-order models for control synthesis. [$z_V = 0$, $\theta_V = 0$, and $\psi_V = 90$ deg]

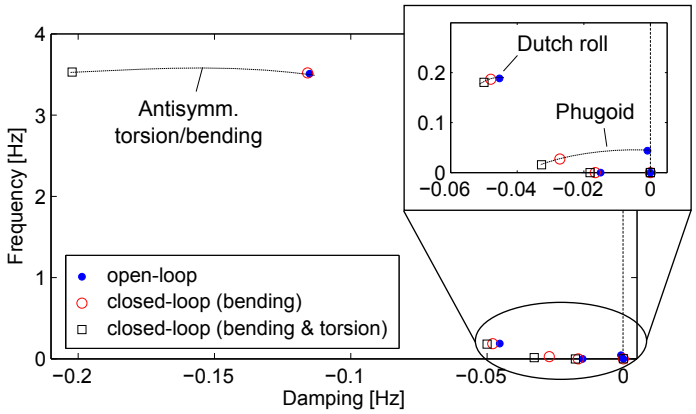
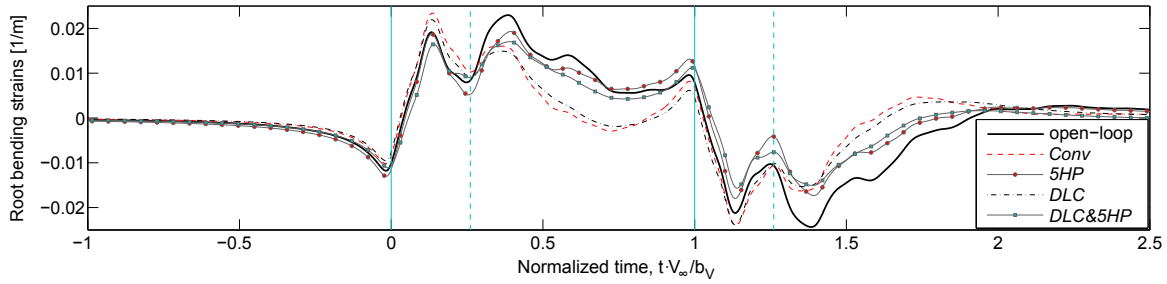



Figure 13: Open- and closed-loop stability characteristics based on the (*Conv*) approach.

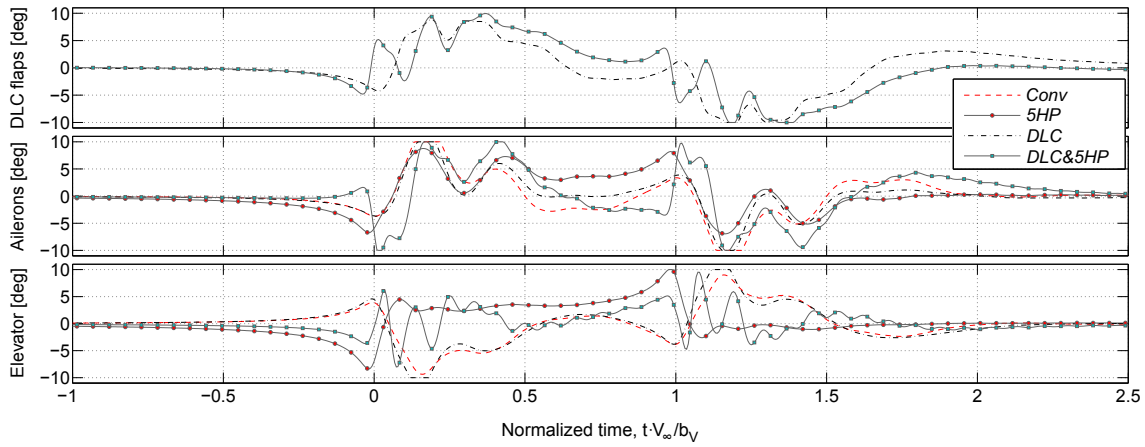
conventional feedback control scheme (*Conv*), that is, alleviation using the existing ailerons and elevator, leads to significant delays in the control surface inputs producing a large overshoot during the fast WVE disturbances. The problem with this first controller is twofold: Firstly, disturbances need to have an effect on the system dynamics so that information reaches the feedback controller through the strain measurements. Secondly, the effectiveness of the ailerons is significantly deteriorated by the flexibility of the main wing, as illustrated in Figure 11. Both issues produce a delay in the control response which can be overcome by using direct disturbance measurements in a feedforward control loop or through DLC flaps, which are less prone to aeroelastic effects in very flexible configurations. In what follows we will analyze the benefits of these two approaches.

To introduce disturbance measurements in a feedforward scheme (*5HP*), we follow the approach outlined in Section 3.2.1, where we use the operator $C_g$ in Eq. (13) to measure the vertical disturbance velocity at the center of the main wing. This could be easily achieved by mounting a 5HP to an existing vehicle configuration [9]. The resulting 2-DOF control scheme responds faster to the external excitations because of the feedforward part which significantly reduces the overshoot and leads to overall reductions of 19% in peak loads, as shown in Figure 14(a).

Next, the use of DLC flaps for load alleviation (*DLC*) has been analyzed first without direct disturbance measurements. The closed-loop response in Figure 14(a) shows that no




(a) Bending strains at root of main wing




(b) Control surface inputs

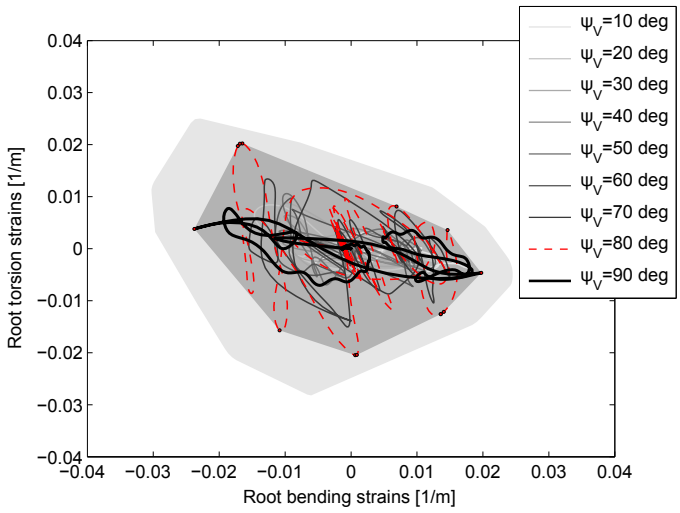
Figure 14: Comparison of different closed-loop WVE reponses with the weightings defined in Table 3. [$z_V = 0$, $\theta_V = 0$, and $\psi_V = 90$ deg]

immediate benefits are obtained to justify the additional weight and complexity of DLC flaps. If combined however with direct measurements of flow disturbances (*DLC&5HP*), significant reductions of 30% of the peak bending strains can be achieved. This confirms the potential of DLC flaps for disturbance compensation, as previously demonstrated in Hahn *et al.* [34] for rigid aircraft, but also highlights the need for preview of the exogenous excitation for such additional control surfaces to be effective.

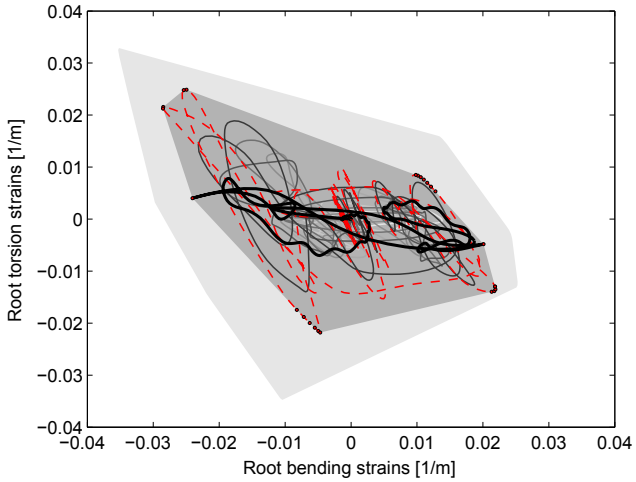
### 4.3.3 Closed-Loop Response at Different Encounter Angles

The open- and closed-loop results in Figure 14 have been obtained using the control model with prescribed flightpaths through wake vortices. To investigate the robustness of the (*DLC&5HP*) control scheme in asymmetric encounter scenarios, Figure 15 shows the closed-loop envelopes for varying encounter angle, $\psi_V$. The closed-loop responses have been obtained by applying the 2-DOF $\mathcal{H}_\infty$ controller with DLC flaps and direct flow measurements to the aeroelastic/flight-dynamic response obtained using the full-order simulation model (including nonlinear flight dynamics). Note that in this case, the flightpath of the encountering aircraft is neither prescribed nor controlled.

Comparison to the corresponding open-loop envelopes from Figure 9, which have been superimposed in Figure 15, show significant reductions of 28% in starboard torsion and 25% in starboard bending strains even for the asymmetric encounter scenarios with possible model mismatch between the linearized, reduced-order control model and the non-




(a) At root of port main wing




(b) At root of starboard main wing

Figure 15: Open- (light gray) and closed-loop (dark gray) envelopes of bending vs. torsion strains for varying encounter angles, $\psi_V$. $[z_V = 0, \theta_V = 0]$

linear simulation plant. Figure 15 further demonstrates that for this vehicle configuration the control problem is not subject to the common trade-off of alleviating either bending or torsion strains [27] because of the stabilizing effect of the combined bending and torsion regulator, as demonstrated in Figure 13.

# 5 Conclusions

Prediction of dynamic loads on flexible aircraft in wake-vortex encounters requires time-domain modeling approaches capable of tracking the trajectory of the encountering vehicle as well as the aerodynamic loads due to the full 3-D disturbance velocity field. In this paper, this was achieved using a coupled flight-dynamics/aeroelastic formulation that retains the gyroscopic couplings between the rigid-body and the structural degrees of freedom, with aerodynamics given by a linearized unsteady vortex lattice method. Numerical

results on a very flexible lightweight platform, representative of a small solar-powered aircraft, show that maximum dynamic loads may occur in asymmetric encounter conditions where rigid-body effects are more prominent.

A linearization of the equations of motion, still written in the physical degrees of freedom (nodal displacements/rotations, vehicle velocities and orientations, and circulations on panels), allows straightforward model reduction using balancing methods. Furthermore, the reduced model retains all individual flow disturbances on the wing collocation points as independent inputs, so that it can be used for simulation in wake encounters. The resulting model is then exercised to investigate different strategies for dynamic load alleviation. It is found, as it was also done previously in the literature, that preview information provides a critical advantage with the fast excitation times that are characteristic of wake encounters. In particular, we show that leading-edge flow measurement devices can be efficiently integrated with a feedforward $\mathcal{H}_\infty$ controller. The loss of efficiency in conventional ailerons, which is due to higher frequency aeroelastic couplings, was also identified, and a solution was proposed based on inboard flaps.

The resulting approach for modeling, simulation and load alleviation in wake encounters can be used from an early stage in the development of new, more flexible air vehicles to assess potential integrity risks and identify mitigating solutions, using either passive or active strategies.

# 6 ACKNOWLEDGEMENT

The authors would like to acknowledge the expert advice by Dr Bing F. Ng, now at Nanyang Technological Insititute, Singapore, in various aspects of the controller design. This work was partially carried while Henrik Hesse was at Imperial College and it is funded by the UK Engineering and Physical Sciences Research Council grant EP/I014683/1.

# References

[1] "Air Traffic Organization Policy," Order JO 7110.308, Federal Aviation Administration (FAA), 2008.

[2] "Aircraft Wake Turbulence," Advisory Circulars AC 90-23G, Federal Aviation Administration (FAA), 2014.

[3] Barbaresco, F., Juge, P., Klein, M., Ricci, Y., Schneider, J., and Moneuse, J., "Optimising runway throughput through wake vortex detection, prediction and decision support tools," *Digital Communications - Enhanced Surveillance of Aircraft and Vehicles*, IEEE, Capri, Italy, Oct. 2011.

[4] Tittsworth, J. A., Lang, S. R., Johnson, E. J., and Barnes, S., "Federal Aviation Administration Wake Turbulence Program – Recent Highlights," *57th Air Traffic Control Association (ATCA) Annual Conference & Exposition*, National Harbor, MD, USA, Oct. 2012.

[5] Pahle, J., Berger, D., Venti, M., Duggan, C., Faber, J., and Cardinal, K., "An Initial Flight Investigation of Formation Flight for Drag Reduction on the C-17 Aircraft," *AIAA Atmospheric Flight Mechanics Conference*, AIAA 2012-4802, Minneapolis, MN, USA, Aug. 2012, doi: 10.2514/6.2012-4802.

[6] Flanzer, T. C., Bieniawski, S. R., and Blake, W. B., "Operational Analysis for the Formation Flight for Aerodynamic Benefit Program," *52nd Aerospace Sciences Meeting at AIAA SciTech 2014*, AIAA 2014-1460, National Harbor, MD, USA, Jan. 2014, doi: 10.2514/6.2014-1460.

[7] Xu, J., Ning, S. A., Bower, G., and Kroo, I., "Aircraft Route Optimization for Formation Flight," *Journal of Aircraft*, Vol. 51, No. 2, 2014, pp. 490–501, doi: 10.2514/1.C032154.

[8] Kienitz, K. H., Kaden, A., and Luckner, R., "Modeling and Design Considerations for Robust Control of Aircraft in Tight Cruise Formation," *AIAA Guidance, Navigation and Control Conference*, AIAA 2013-4858, Boston, MA, USA, 2013, doi: 10.2514/6.2013-4858.

[9] Hahn, K.-U. and Schwarz, C., "Alleviation of Atmospheric Flow Disturbance Effects on Aircraft Response," ICAS Paper 2008-5.2.2, Anchorage, Alaska, USA.

[10] Burnham, D. C. and Hallock, J. N., "Chicago Monostatic Acoustic Vortex Sensing System," Tech. rep., National Information Service, Springfield, VA, USA, 1982.

[11] Devenport, W. J., Rife, M. C., Liapis, S. I., and Follin, G. J., "The structure and development of a wing-tip vortex," *Journal of Fluid Mechanics*, Vol. 312, 1996, pp. 67–106, doi: 10.1017/S0022112096001929.

[12] Holzäpfel, F., Misaka, T., and Hennemann, I., "Wake-vortex topology, circulation, and turbulent exchange processes," *AIAA Atmospheric and Space Environments Conference*, AIAA 2010-7992, Toronto, ON, Canada, 2010, doi: 10.2514/6.2010-7992.

[13] Bieniek, D. and Luckner, R., "Simulation of Aircraft Encounters with Perturbed Vortices Considering Unsteady Aerodynamic Effects," *Journal of Aircraft*, Vol. 51, No. 3, 2014, pp. 705–718, doi: 10.2514/1.C032383.

[14] Fischenberg, D., "A method to validate wake vortex encounter models from flight test data," *27$^{th}$ International Congress of the Aeronautical Sciences*, Nice, France, 2010.

[15] Hahn, K.-U. and Schwarz, C., "Safe Limits for Wake Vortex Penetration," *AIAA Guidance, Navigation and Control Conference*, AIAA 2007-6871, Hilton Head, SC, USA, 2007.

[16] Climent, H., Lindenau, O., Claverías, S., Viana, J. T., Oliver, M., Benitez, L., Pfeifer, D., and Jenaro-Rabadan, G., "Flight Test Validation of Wake Vortex Encounter Loads," *International Forum on Aeroelasticity and Structural Dynamics*, IFASD 2013-27B, Bristol, UK, June 2013.

[17] Kier, T. M., "An Integrated Loads Analysis Model Including Unsteady Aerodynamic Effects for Position and Attitude Dependent Gust Fields," *International Forum on Aeroelasticity and Structural Dynamics*, IFASD 2011-052, Paris, France, June 2011.

[18] Kier, T. M., "An Integrated Loads Analysis Model for Wake Vortex Encounters," *International Forum on Aeroelasticity and Structural Dynamics*, IFASD 2013-30C, Bristol, UK, June 2013.

[19] Karpel, M., Shousterman, A., Climent, H., and Reyes, M., "Dynamic Response to Wake Encounter," *54th AIAA Structures, Structural Dynamics, and Materials Conference*, AIAA 2013-1921, Boston, MA, USA, 2013, doi: 10.2514/6.2013-1921.

[20] Karpel, M., "Procedures and Models for Aeroservoelastic Analysis and Design," *ZAMM - Journal of Applied Mathematics and Mechanics / Zeitschrift für Angewandte Mathematik und Mechanik*, Vol. 81, No. 9, 2001, pp. 579–592, doi: 10.1002/1521-4001(200109)81:9¡579::AID-ZAMM579¿3.0.CO;2-Z.

[21] Claverías, S., Cerezo, J., Torralba, M. A., Reyes, M., Climent, H., and Karpel, M., "Wake Vortex Encounter Loads Numerical Simulation," *International Forum on Aeroelasticity and Structural Dynamics*, IFASD 2013-30B, Bristol, UK, June 2013.

[22] Murua, J., Palacios, R., and Graham, J., "Applications of the unsteady vortex-lattice method in aircraft aeroelasticity and flight dynamics," *Progress in Aerospace Sciences*, Vol. 55, Nov. 2012, pp. 46–72, doi: 10.1016/j.paerosci.2012.06.001.

[23] Patil, M. J., Hodges, D. H., and Cesnik, C. E., "Nonlinear aeroelasticity and flight dynamics of high-altitude long-endurance aircraft," *Journal of Aircraft*, Vol. 38, No. 1, 2001, pp. 88–94.

[24] Su, W. and Cesnik, C., "Nonlinear Aeroelasticity of a Very Flexible Blended-Wing-Body Aircraft," *Journal of Aircraft*, Vol. 47, No. 5, 2010, pp. 1539–1553.

[25] Hesse, H. and Palacios, R., "Reduced-Order Aeroelastic Models for Dynamics of Maneuvering Flexible Aircraft," *AIAA Journal*, Vol. 52, No. 8, 2014, pp. 1717–1732, doi: 10.2514/1.J052684.

[26] Hesse, H., Palacios, R., and Murua, J., "Consistent Structural Linearization in Flexible Aircraft Dynamics with Large Rigid-Body Motion," *AIAA Journal*, Vol. 52, No. 3, 2014, pp. 528–538, doi: 10.2514/1.J052316.

[27] Cook, R. G., Palacios, R., and Goulart, P., "Robust Gust Alleviation and Stabilization of Very Flexible Aircraft," *AIAA Journal*, Vol. 51, No. 2, February 2013, pp. 330–340, doi: 10.2514/1.J051697.

[28] Dillsaver, M., Cesnik, C., and Kolmanovsky, I., "Gust Load Alleviation Control for Very Flexible Aircraft," *AIAA Atmospheric Flight Mechanics Conference*, AIAA 2011-6368, Portland, OR, USA, Aug. 2011, doi: 10.2514/6.2011-6368.

[29] Simpson, R. J. S., Palacios, R., Hesse, H., and Goulart, P. J., "Predictive Control for Alleviation of Gust Loads on Very Flexible Aircraft," *55th AIAA Structures, Structural Dynamics, and Materials Conference*, National Harbor, Maryland, USA, 2014, AIAA Paper No. 2014-0843.

[30] Robinson, P. A., "Use of predictive lidar measurements in alleviating turbulence-induced disturbances of aircraft in flight," *Proc. SPIE 2737*, Orlando, FL, USA, 1996, pp. 86–97, doi: 10.1117/12.241056.

[31] Rahm, S., Smalikho, I., and Köpp, F., "Characterization of Aircraft Wake Vortices by Airborne Coherent Doppler Lidar," *Journal of Aircraft*, Vol. 44, No. 3, 2007, pp. 799–805, doi: 10.2514/1.24401.

[32] Wildschek, A., Haniš, T., and Stroscher, F., "$\mathcal{L}_\infty$-Optimal feedforward gust load alleviation design for a large blended wing body airliner," *Progress in Flight Dynamics, GNC, and Avionics*, Vol. 6, 2013, pp. 707–728, doi: 10.1051/eucass/201306707.

[33] Giesseler, H.-G., Kopf, M., Faulwasser, T., Varutti, P., and Findeisen, R., "Gust Load Alleviation Based on Model Predictive Control," *International Forum on Aeroelasticity and Structural Dynamics*, IFASD 2013-24A, Bristol, UK, June 2013.

[34] Hahn, K.-U., Fischenberg, D., Niedermeier, D., and Horn, C., "Wake Encounter Flight Control Assistance Based on Forward-Looking Measurement Processing," *AIAA Guidance, Navigation, and Control Conference*, AIAA 2010-7680, Toronto, Ontario, Canada, 2010, doi: 10.2514/6.2010-7680.

[35] Schwarz, C. and Hahn, K. U., "Automated pilot assistance for wake vortex encounters," *Aerospace Science and Technology*, Vol. 15, No. 5, 2011, pp. 416–421, doi: 10.1016/j.ast.2010.09.008.

[36] Westermayer, C., Schirrer, A., Hemedi, M., and Kozek, M., "An $\mathcal{H}_\infty$ full information approach for the feedforward controller design of a large blended wing body flexible aircraft," *Progress in Flight Dynamics, GNC, and Avionics*, Vol. 6, 2013, pp. 685–706, doi: 10.1051/eucass/201306685.

[37] Murua, J., Palacios, R., and Graham, J. M. R., "Assessment of Wake-Tail Interference Effects on the Dynamics of Flexible Aircraft," *AIAA Journal*, Vol. 50, No. 7, July 2012, pp. 1575–1585, doi: 10.2514/1.J051543.

[38] Hesse, H. and Palacios, R., "Consistent structural linearisation in flexible-body dynamics with large rigid-body motion," *Computers & Structures*, Vol. 110–111, 2012-11, pp. 1–14, doi: 10.1016/j.compstruc.2012.05.011.

[39] Hall, K., "Eigenanalysis of Unsteady Flows about Airfoils, Cascades and Wings," *AIAA Journal*, Vol. 32, No. 12, 1994, pp. 2426–2432.

[40] Simpson, R. J. S., Palacios, R., and Murua, J., "Induced Drag Calculations in the Unsteady Vortex-Lattice Method," *AIAA Journal*, Vol. 51, No. 7, 2013, pp. 1775–1779, doi: 10.2514/1.J052136.

[41] Simo, J. C. and Vu-Quoc, L., "On the dynamics in space of rods undergoing large motions - A geometrically exact approach," *Computer Methods in Applied Mechanics and Engineering*, Vol. 66, No. 2, 1988, pp. 125–161, doi: 10.1016/0045-7825(88)90073-4.

[42] Géradin, M. and Cardona, A., *Flexible multibody dynamics: a finite element approach, Chapter 6*, John Wiley & Sons Ltd, Chichester, UK, 2001.

[43] Stevens, B. L. and Lewis, F. L., *Aircraft Control and Simulation, Chapter 1*, John Wiley & Sons, Inc., New York, NY, USA, 1992.

[44] Géradin, M. and Rixen, D., *Mechanical Vibrations: Theory and Application to Structural Dynamics, Chapter 7*, John Wiley & Sons Ltd, Chichester, UK, 2nd ed., 1997.

[45] Murua, J., Palacios, R., and Graham, J. M. R., "Open-Loop Stability and Closed-Loop Gust Alleviation on Flexible Aircraft Including Wake Modeling," *53rd AIAA Structures, Structural Dynamics, and Materials Conference*, AIAA 2012-1484, Honolulu, HI, USA, 2012.

[46] Loucel, R. E. and Crouch, J. D., "Flight-Simulator Study of Airplane Encounters with Perturbed Trailing Vortices," *Journal of Aircraft*, Vol. 42, No. 4, 2005, pp. 924–931, doi: 10.2514/1.8556.

[47] Katz, J. and Plotkin, A., *Low-Speed Aerodynamics, Chapter 2*, Cambridge Aerospace Series, Cambridge University Press, New York, NY, USA, 2nd ed., 2001.

[48] Rosenhead, L., "Formation of Vortices from a Surface of Discontinuity," *Proceedings Royal Society of London*, Vol. 134, London, UK, 1931, p. 170–192.

[49] Lamb, H., "Hydrodynamics," *Hydrodynamics*, Cambridge University Press, Cambridge, UK, 1932, pp. 590–592.

[50] Moore, B., "Principal component analysis in linear systems: Controllability, observability, and model reduction," *IEEE Transactions on Automatic Control*, Vol. 26, No. 1, Feb. 1981, pp. 17–32, doi: 10.1109/TAC.1981.1102568.

[51] Glover, K., "All optimal Hankel-norm approximations of linear multivariable systems and their $L^\infty$-error bounds," *International Journal of Control*, Vol. 39, No. 6, 1984, pp. 1115–1193, doi: 10.1080/00207178408933239.

[52] van den Kroonenberg, A., Martin, T., Buschmann, M., Bange, J., and Vörsmann, P., "Measuring the Wind Vector Using the Autonomous Mini Aerial Vehicle M$^2$AV," *Journal of Atmospheric and Oceanic Technology*, Vol. 25, No. 11, Nov. 2008, pp. 1969–1982, doi: 10.1175/2008JTECHA1114.1.

[53] Skogestad, S. and Postlethwaite, I., *Multivariable feedback control: analysis and design, Chapter 2*, John Wiley & Sons Ltd, Chichester, UK, 2005.

[54] Limebeer, D. J. N., Kasenally, E. M., and Perkins, J. D., "On the design of robust two degree of freedom controllers," *Automatica*, Vol. 29, No. 1, Jan. 1993, pp. 157–168, doi: 10.1016/0005-1098(93)90179-W.

[55] Balas, G., Chiang, R., Packard, A., and Safonov, M., *Robust Control Toolbox User's Guide*, The MathWorks, Inc., Natick, MA, USA, 2006.

[56] Doyle, J., Glover, K., Khargonekar, P., and Francis, B., "State-space solutions to standard H2 and H infin; control problems," *IEEE Transactions on Automatic Control*, Vol. 34, No. 8, Aug. 1989, pp. 831–847, doi: 10.1109/9.29425.

[57] Palacios, R., Murua, J., and Cook, R., "Structural and Aerodynamic Models in the Nonlinear Flight Dynamics of Very Flexible Aircraft," *AIAA Journal*, Vol. 48, No. 11, 2010, pp. 2559–2648, doi: 10.2514/1.52446.

[58] "The Code of Federal Regulations of the United States of America, Title 14: Aeronautics and Space, Part 25 – Airworthiness Standards: Transport Category Airplanes," 2007.

# 7 COPYRIGHT STATEMENT

The authors confirm that they give permission for the publication and distribution of this paper as part of the IFASD 2015 proceedings or as individual off-prints from the proceedings.